ADVANCED FUNCTIONAL MATERIALS
www.afm-journal.de

High-Entropy Doped $KTiOPO_4$-Type Vanadium-Based Fluorophosphate Cathodes for High-Energy Sodium-Ion Batteries

*Yingkai Hua, Zizheng Song, Kunran Yang, Seungjae Suk, Linlong Lyu, Xiangjun Pu, Renjie Li, Haitao Huang, Kyu-Young Park, Zibin Chen, and Zheng-Long Xu**

The development of high-energy-density and high-power cathode materials represents a critical requirement for advancing practical sodium-ion battery (SIB) technologies. In this work, a high-entropy-doped $KTiOPO_4$ (KTP)-type $NaV_{0.95}(Fe, Mn, Ni, Al, Ca)_{0.05}PO_4F$ (HE-NVPF) cathode material is presented, designed to enhance reaction kinetics, operation voltage, and energy density through single-crystal phase formation and improved electronic/ionic conductivity. The high-entropy doping strategy enables the elimination of inductive nucleation agents while promoting single-crystal growth of HE-NVPF during low-temperature hydrothermal synthesis. The KTP-type crystal structure facilitates complete Na ion utilization and enables a solid-solution Na storage mechanism in HE-NVPF cathodes, accompanied by minimal lattice volume changes (4%). When tested in half cells in combination with Na metal anode, the HE-NVPF cathodes exhibit a remarkably high energy density of 532 Wh kg^{-1} with an average operating voltage of 4.0 V, an exceptional long cycle life of 3 000 cycles, and high capacity retentions at 30 C (2 min per charge). Its practical feasibility is demonstrated in graphite//HE-NVPF full cells, which present power densities of above 10 000 W kg^{-1} and energy densities of over 342 Wh kg^{-1} for 1000 cycles. This work offers new insights into designing high-entropy doped cathode materials for long-life and fast-charging SIBs.

1. Introduction

Sodium-ion batteries (SIBs) have garnered significant interest as a promising alternative to lithium-ion batteries, primarily due to the high abundance and low cost of sodium resources.[1] The performance of SIBs is heavily dependent on the choice of cathode materials, which include transition-metal layered oxides,[2] Prussian blue analogues,[3] and polyanionic compounds.[4] Among these, polyanionic compounds are particularly noteworthy for their excellent structural stability and long-term cycling performance. In this category, sodium (Na) super ionic conductor (NASICON)-type polyanionic compounds, characterized by an open 3D framework and rapid Na^+ ion diffusion capability, stand out. However, the presence of heavy phosphate blocks in NASICON materials often results in moderate capacities and energy densities. For example, $Na_3V_2(PO_4)_3$ (NVP) exhibits reversible capacities of ≈110 mAh g^{-1} and operating

Y. Hua, Z. Song, L. Lyu, X. Pu, R. Li, Z. Chen, Z.-L. Xu
Research Institute for Advanced Manufacturing
Department of Industrial and Systems Engineering
The Hong Kong Polytechnic University
Hung Hom, Hong Kong SAR 999077, China
E-mail: zhenglong.xu@polyu.edu.hk

K. Yang
School of Physical Science and Technology
ShanghaiTech University
Shanghai 201210, China

S. Suk, K.-Y. Park
Graduate Institute of Ferrous & Energy Materials Technology
Pohang University of Science and Technology (POSTECH)
Pohang 37667, Republic of Korea

X. Pu
Department of Materials Science and Engineering
Seoul National University
Seoul 08826, Republic of Korea

H. Huang
Department of Applied Physics
The Hong Kong Polytechnic University
Hung Hom, Hong Kong SAR 999077, China

H. Huang, Z.-L. Xu
Research Institute for Smart Energy
The Hong Kong Polytechnic University
Hung Hom, Hong Kong SAR 999077, China

The ORCID identification number(s) for the author(s) of this article can be found under https://doi.org/10.1002/adfm.202512341

DOI: 10.1002/adfm.202512341

voltages of ≈3.4 V.[5] In addition, the stoichiometric ratio of Na:V = 3:2 in NVP hinders the full extraction of three Na ions[4a] due to high overpotentials and substantial lattice distortion associated with removing the 3rd Na ion,[6] further limiting the specific capacities and energy densities.

$KTiOPO_4$-type $NaVPO_4F$ (KTP-type NVPF) cathode materials, characterized by their orthorhombic structure and large spaces along the [100] and [010] directions for Na ion accommodation, offer great potential for complete Na^+ extraction.[4b,7] Theoretical capacity of 143 mAh g^{-1}, which is 10% higher than that for NVP structures, is achievable due to the one-to-one correspondence between Na ion insertion and *d*-metal cation redox in the $NaVPO_4F$ formula. However, KTP-type NVPF cathodes face challenges such as phase impurities during synthesis, low intrinsic electronic conductivity, and phase separation during cycling.[8] Conventional solid-state synthesis methods often fail to produce phase-pure KTP-type NVPF, while strategies to enhance electronic conductivity typically rely on excessive carbon coating, which complicates synthesis and diminishes practical capacities.[9] High-entropy doping has emerged as a promising approach to improve structural stability and ionic/electronic conductivity by tailoring the local atomic environment.[10] Despite its potential, this strategy remains unexplored for KTP-type NVPF. Previous studies on high-entropy doping in NVP cathodes employed substantial doping concentrations (≈50 at.%), often at the expense of capacity.[10c,h,i] In contrast, trace doping (≤5 at.%) of heterogeneous elements could effectively enhance the performance of high-energy KTP-type NVPF, though this avenue remains underexplored.

In this work, we introduce a carbon-free high-entropy $NaV_{0.95}(Fe, Mn, Ni, Al, Ca)_{0.05}PO_4F$ (HE-NVPF) cathode via a facile hydrothermal and ion-exchange method. By incorporating heterogeneous dopant precursors, we eliminate the need for conventional nucleation agents (e.g., carboxymethyl cellulose, CMC-Na), yielding a carbon-free structure. Combined theoretical and experimental analyses demonstrate that HE-NVPF exhibits enhanced electronic/ionic conductivity, superior structural integrity, and full Na ion utilization. In situ X-ray diffraction (XRD) characterizations indicate a solid-solution phase evolution during Na-ion insertion and extraction reactions, contrasting with the biphasic reaction for pristine KTP-type NVPF. The lattice volume changes are calculated to be below 4% during Na insertion, providing a testament to its excellent stability. In Na-ion half cells consisting of Na metal anodes and 1 M $NaPF_6$ carbonate electrolyte, the HE-NVPF demonstrates excellent electrochemical performance with an elevated operating voltage of 4.0 V and a high energy density of 532 Wh kg^{-1} at 0.1 C (1 C = 143 mA g^{-1}), in comparison to the 3.75 V and 413 Wh kg^{-1} for pristine NVPF. Furthermore, when paired with graphite anodes into Na-ion full cells, the HE-NVPF cathodes show outstanding energy and power densities of over 342 Wh kg^{-1} and 10 000 W kg^{-1} (capacity retention of ≈99% after 1000 cycles), highlighting its practical application for fast-charging and long-life SIBs.

2. Results and Discussion

The HE-NVPF cathode material was prepared via a hydrothermal and ion-exchange method. In particular, the $NH_4V_{0.95}(Fe, Mn, Ni, Al, Ca)_{0.05}PO_4F$ precursor was synthesized by hydrothermal reaction, which then reacted with sodium glutamate to form $NaV_{0.95}(Fe, Mn, Al, Ca)_{0.05}PO_4F$ through an ion-exchange process. Pristine NVPF (p-NVPF) was also synthesized using similar methods for comparison. **Figure 1**a,b show the XRD patterns and refinement results for HE-NVPF and p-NVPF structures, which indicate phase-pure orthorhombic units with the Pna21 space group. This configuration contains interlinking chains of P-O tetrahedra and HE/VO_4F_2 octahedra through corner-shared oxygen atoms, where the fluorine atoms occupy two cis-/trans-positions near the vanadium (V) atoms. The Fe, Mn, Ni, Al, and Ca dopants (i.e., stoichiometric 5% of V) replaced V cations at the V1 and V2 sites without detectable impurities in the XRD patterns (Figure 1a). Refinement-derived lattice parameters reveal a slight lattice expansion in HE-NVPF (850.028 $Å^3$) compared to p-NVPF (846.960 $Å^3$; Table S1, Supporting Information), attributable to the larger ionic radii of dopants (e.g., V^{3+}: 0.64 Å; Fe^{2+}: 0.78 Å; Ni^{2+}: 0.69 Å; Ca^{2+}: 1.00 Å).[11] Notably, a carboxymethyl cellulose (CMC-Na) nucleation agent was necessary to synthesis phase-pure p-NVPF. CMC-Na facilitates the nucleation of NH_4VPO_4F from the solution by forming linkages with V metal ions through its abundant carboxylic acid and hydroxyl groups, thereby creating uniform nucleation sites.[12] As shown in Figure S1 (Supporting Information), amorphous NH_4VPO_4F particles grew on the surface of the CMC-Na fibers after 2 h of hydrothermal reaction, substantiating its role as a nucleation promoter. Otherwise, noticeable impurities appear, as shown in the XRD patterns (Figure S2, Supporting Information). The NVPF prepared in CMC-Na absent conditions presents porous and irregular morphology (Figure S3, Supporting Information). With CMC-Na precursors, the surface layer of p-NVPF can be reduced into carbon coating layers, e.g., 12.3 wt.% of carbon in thermogravimetry analysis (TGA) result (Figure 1c) and the high-angle annular dark-field scanning transmission electron microscopy (HAADF-STEM) image and energy dispersive X-ray spectroscopy (EDS) mapping results (Figure S4, Supporting Information). In contrast, the incorporation of Ni^{2+}, Mn^{2+}, and Ca^{2+} metal ions can facilitate the nucleation dynamics for synthesizing carbon-free HE-NVPF material (Figure S5, Supporting Information). The abundant metal ions facilitated the individual nucleation and single-crystal growth of NH_4VPO_4F precursor during the hydrothermal reaction (Figure S6, Supporting Information).

Scanning electron microscope (SEM) images exhibit well-shaped blocky rhombohedral particles for HE-NVPF and p-NVPF (Figure S7, Supporting Information), implying their high crystallinity and phase purity. Figure S8 (Supporting Information) presents the general X-ray photoelectron spectroscopy (XPS) spectra for HE-NVPF and p-NVPF. It is observed that the peak intensity of N 1s is much higher in p-NVPF than HE-NVPF, possibly due to the incomplete Na^+/NH_4^+ ion-exchange for carbon-coated NH_4VPO_4F precursor. The V:Na ratio in p-NVPF was determined as 1:0.7743 by ICP-OES test, again demonstrating the incomplete Na^+/NH^{4+} ion-exchange. The V 2p peak can be deconvoluted into two group peaks at 516.51/516.02 eV and 523.89/523.40 eV for the V $2p_{3/2}$ and V $2p_{1/2}$ orbits (Figure S9, Supporting Information), corresponding to the V^{3+} valence state.

Figure 1d presents the integrated differential phase contrast–scanning transmission electron microscopy (iDPC-STEM) image of HE-NVPF along the [100] zone axis. The image distinctly reveals the alternating layers of HE/VO_4F_2 octahedra and

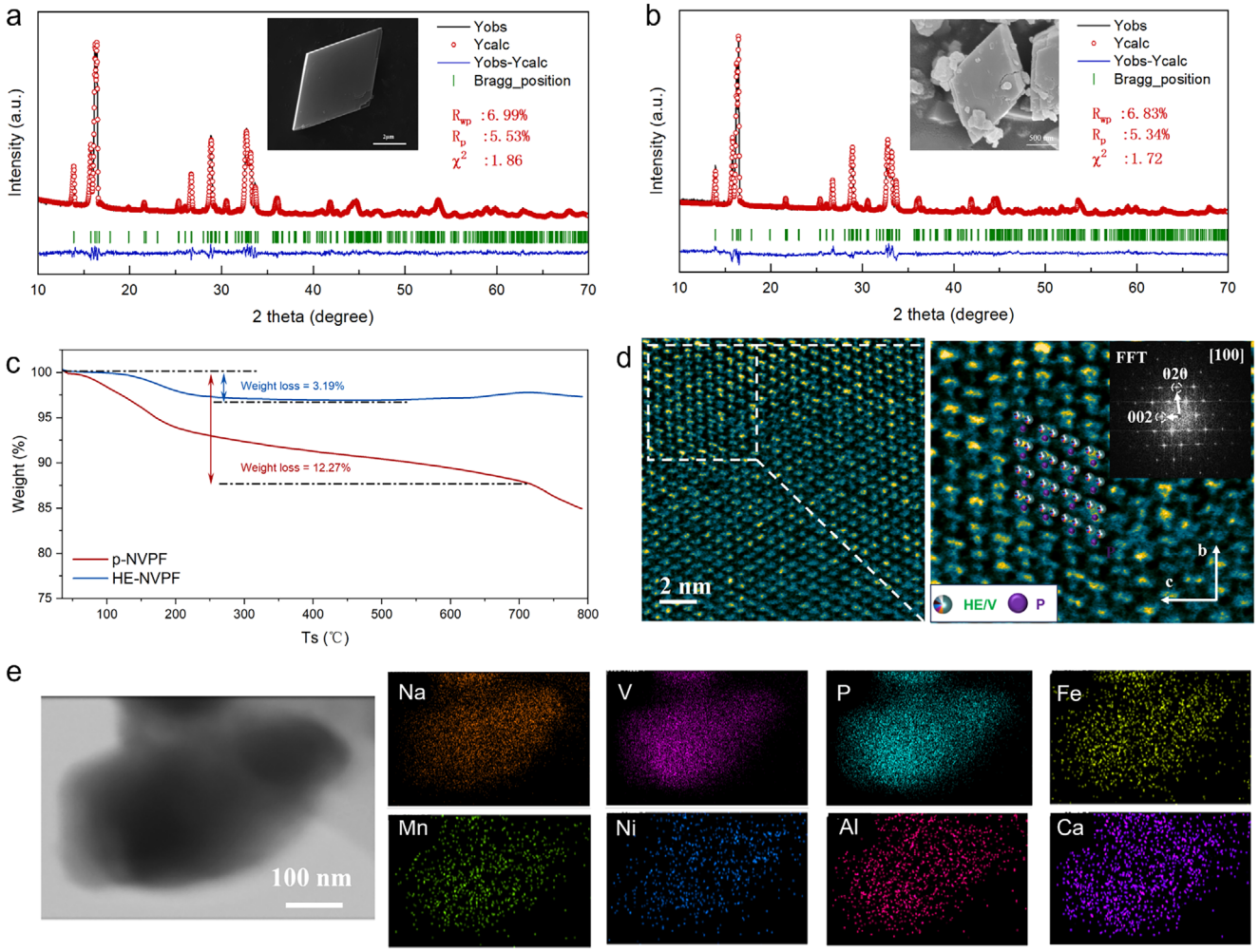

Figure 1. Structural and morphology characterization of HE-NVPF. XRD Rietveld refinement results and SEM images (inset) a) HE-NVPF and b) p-NVPF, c) TGA curves of HE-NVPF and p-NVPF, d) iDPC-STEM image and corresponding FFT diffraction pattern of HE-NVPF, e) BF-STEM image and corresponding EDS mappings of HE-NVPF.

phosphorus tetrahedra within the crystal structure. The corresponding fast Fourier transform (FFT) pattern exhibits distinct (020) and (002) diffraction spots, which align well with the expected lattice structure.[4b] Figure 1e shows a bright-field scanning transmission electron microscopy (BF-STEM) image of a HE-NVPF particle and the corresponding EDS mapping images. The Fe, Mn, Ni, Al, and Ca doping elements are uniformly distributed among the Na, V, and P parent hosts, indicating their homogeneous substitution without aggregations. This uniform doping is further corroborated by SEM-EDS analyses of both the $NH_4V_{0.95}$(Fe, Mn, Ni, Al, Ca)$_{0.05}PO_4F$ precursor and HE-NVPF product (Figures S10 and S11, Supporting Information). The elemental ratio was investigated via inductively coupled plasma-optical emission spectroscopy (ICP-OES), which confirmed the dopant elements in HE-NVPF cathodes (Table S2, Supporting Information).

The electrochemical performance of HE-NVPF and p-NVPF cathode materials was evaluated in coin cells with Na metal anodes and 1 M $NaPF_6$ EMC:FEMC:FEC (2:3:5) electrolyte. In order to demonstrate the necessity of trace metal ions doping strategy, a comparison of different doping concentrations is exhibited in Figure S12 (Supporting Information). As doping concentrations increase from 5 to 50 at.%, the discharge capacity progressively decreases, suggesting the electrochemical inactivity of the dopants. The galvanostatic charge–discharge curves of HE-NVPF present no distinctive plateaus, possibly due to the high-entropy effect.[10f,3a] HE-NVPF cathode delivers a discharge capacity of 133 mAh g^{-1} at 0.1 C (1 C is defined as the current density for fully charging in 1 h) with an average operating voltage of 4.0 V, resulting in a competitive energy density of 532 Wh kg^{-1} (**Figure 2a**). Voltage profiles over the first ten cycles present negligible capacity and voltage degradations, highlighting the excellent reversibility for HE-NVPF. In contrast, the charge–discharge profile of p-NVPF cathode exhibits large voltage hysteresis and a lower capacity, thus rendering an inferior energy density of 413 Wh kg^{-1} (Figure S13, Supporting Information). The discharge profiles and differential capacity/voltage (dQ/dV) plots in Figure 2b,c show a relatively lower operating voltage of 3.75 V for p-NVPF than that for HE-NVPF. The capacity contributions above 4.1 V are 40.35% for HE-NVPF and 30.89%

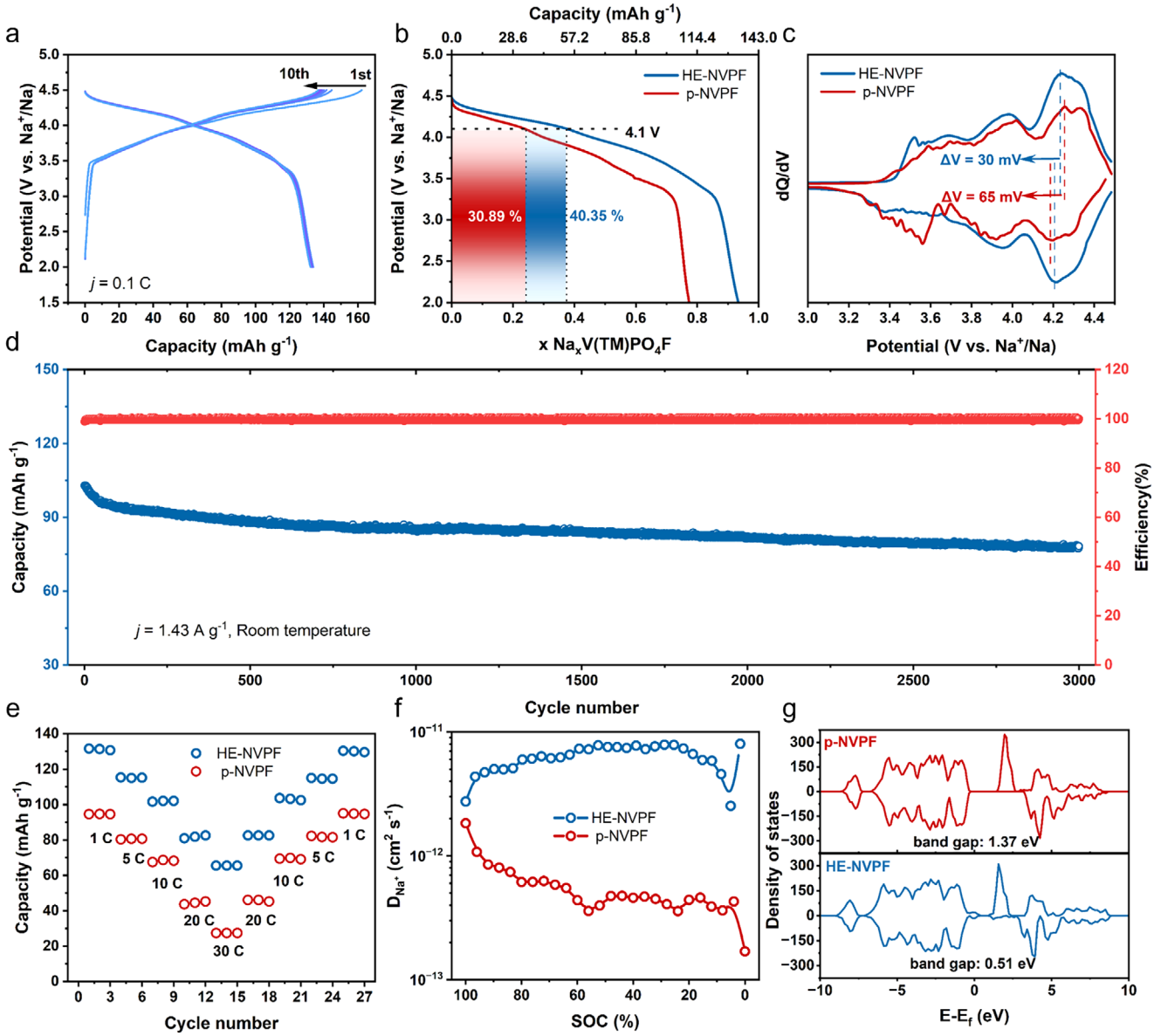

Figure 2. a) The charge–discharge voltage profiles at 0.1 C for HE-NVPF. b) Proportion of high voltage region (>4.1 V) of HE-NVPF and p-NVPF. c) dQ/dV curves from the 3rd cycle for HE-NVPF and p-NVPF. d) Cycling performance at 10 C of HE-NVPF. e) Rate capability from 1 to 30 C for HE-NVPF and p-NVPF. f) Diffusion coefficient of HE-NVPF and p-NVPF at different SOC. g) Total density of states for p-NVPF and HE-NVPF.

for p-NVPF, representing the high-voltage energy contribution for HE-NVPF. A discharging plateau at ≈3.5 V was identified for p-NVPF (Figure 2b), possibly arising from phase separation near the end of Na insertion.[4b] The voltage hysteresis between discharging and charging peaks in Figure 2c is 65 mV for p-NVPF and 30 mV for HE-NVPF, implying enhanced reaction kinetics due to high-entropy doping.

Long-term cycling stability is crucial for practical cathodes in SIBs. An extended cycling test at a high current rate of 10 C for 3000 cycles (Figure 2d) shows that HE-NVPF maintains reversible capacities of 102.8 and 77.4 mAh g^{-1} at the 1st and 3000th cycles, respectively, leading to an extremely low capacity degradation rate of 0.008% per cycle. The exceptional cyclability of HE-NVPF can be attributed to the structural robustness, as evidenced by the SEM image in Figure S14 (Supporting Information) of cycled HE-NVPF.

To further evaluate the improved Na ion storage kinetics from high-entropy doping, HE-NVPF and p-NVPF cathodes were subjected to a series of electrochemical characterizations. The rate capability of HE-NVPF and p-NVPF were measured at increasing current rates from 1 to 30 C (Figure 2e). The HE-NVPF cathode delivers a decent capacity retention of 47% from 131.37 mAh g^{-1} at 1 C to 65.55 mAh g^{-1} at 30 C (corresponding to 2 min per charge), indicating the fast-charging capability of HE-NVPF. In contrast, the p-NVPF cathode delivers significantly lower discharging capacities of 94.73 mAh g^{-1} at 1 C and 27.41 mAh g^{-1} at 30 C. The $D_{Na}{}^{+}$ values were calculated using the galvanostatic intermittent titration technique (GITT) measurement at

different state-of-charge (SOC). HE-NVPF delivered an average D_{Na}^+ of 6×10^{-12} cm^2 s^{-1}, which is 10 times higher than those for p-NVPF (Figure 2f). The D_{Na}^+ of HE-NVPF cathode remains relatively stable during the whole charging process, whereas the p-NVPF cathode exhibits low D_{Na}^+ in the low SOC region. The significantly low Na^+ ion diffusion coefficient for p-NVPF can be attributed to the absence of a high-entropy effect and the remaining NH_4^+ ions at Na ion sites, which warrant in-depth investigations in future study. DFT calculated total density of states (DOS) for HE-NVPF and p-NVPF (Figure 2g) show a substantially reduced bandgap for HE-NVPF (0.51 eV) compared to p-NVPF (1.27 eV). It means electron excitation from the valence to the conduction band is easier in HE-NVPF. Furthermore, the projected density of states (PDOS) of vanadium present a lower V^{3+}/V^{4+} redox energy for HE-NVPF than p-NVPF, which indicates a higher operation voltage of the HE-NVPF cathode (Figure S15, Supporting Information).[13] The improvements in electronic and ionic conductivities are believed to contribute to the high-rate performance of carbon-free HE-NVPF cathodes.

The Na ion storage mechanisms in HE-NVPF were investigated by in situ XRD characterizations. **Figure 3a** shows the in situ XRD patterns of HE-NVPF cathode cycling at 0.15 C for the first cycle, with data collected in the range of 13°–45°. Figure S16 (Supporting Information) presents the evolution of representative peaks corresponding to (200), (011), and (002) planes during the charging process. A rightward shift of these peaks corresponds to the lattice contraction during Na ion extraction, while their return to original positions during the following discharge suggests a reversibility of the HE-NVPF structure. The absence of new peaks throughout the whole charging and discharging processes indicates a solid-solution phase evolution for HE-NVPF cathodes. In contrast, p-NVPF shows a new peak at 33.7° during the discharging process at a voltage range of 3.7–3.4 V, implying phase separation or bi-phasic reaction for p-NVPF structure in the low-voltage discharging plateau (Figure S17, Supporting Information), as previously reported.[4b] Compared to biphasic reaction, solid-solution phase evolution enhances the reaction kinetics and structural stability in cathodes. In addition, the lattice parameters of HE-NVPF at different charge/discharge states were calculated from the in situ XRD patterns (Figure 3b). The *a*, *b*, and *c*-spacing contract by 1.3%, 1.1%, and 1.7% during charging (Figure 3c), leading to a volume change (ΔV) of 4%. The marginal volume change can indicate low-strain and high structural stability for HE-NVPF cathodes.[14]

The local structure evolution and valence state changes of redox centers were examined by X-ray absorption spectroscopy (XAS). Figure 3d shows the V K-edge X-ray absorption near-edge spectroscopy (XANES) results. Both fresh HE-NVPF and p-NVPF cathodes present V absorption edges close to that of V_2O_3, indicating a near V^{3+} valence state. Upon charging to 4.5 V, the V K-edge XANES spectra shift to higher energy values close to that of VO_2, which demonstrates the oxidation of V^{3+} to V^{4+} during desodiation. Notably, the V K-edge of HE-NVPF is ≈1 eV higher than that of charged p-NVPF and is closer to the V^{4+} state, which can be interpreted by the incomplete desodiation of p-NVPF (Figure 2b). The pre-edge features of V K-edge XANES spectra are sensitive to the valence and local structure.[15] Figure S18 (Supporting Information) shows the pre-edge peaks of the fresh and the 1st cycled HE-NVPF. The peak intensities are almost intact

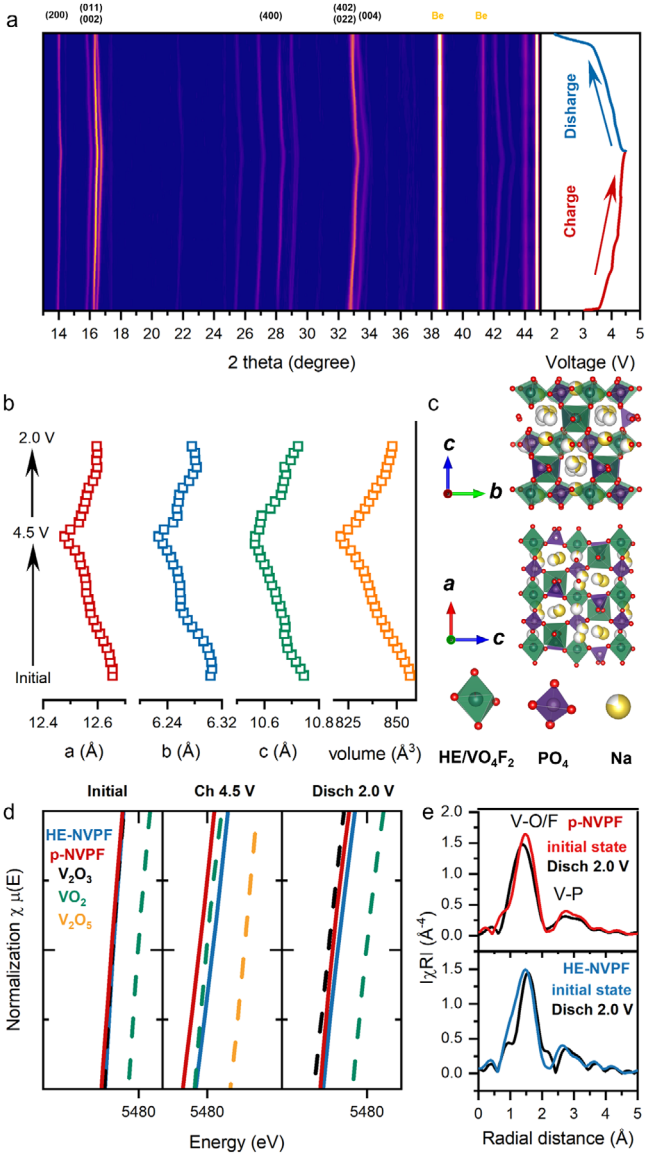

Figure 3. Structural evolutions and redox mechanisms of HE-NVPF and p-NVPF. a) In situ XRD patterns of HE-NVPF during the 1st cycle. b) Calculated lattice parameters of HE-NVPF from in situ XRD patterns. c) Schematic illustration of HE-NVPF lattice structures. d) V K-edge XANES at different charge/discharge state. e) EXAFS spectra of p-NVPF (top) and HE-NVPF (down) at initial and discharged states.

due to the negligible structure distortion in HE/VO_4F_2 octahedra. In contrast, the pre-edge peaks at 5467.8 and 5469.4 eV for fresh p-NVPF changed to a single peak located at 5469.4 eV, possibly due to the local distortion of VO_4F_2 octahedra after charging.[15c] Figure 3e presents the extended X-ray absorption fine structure (EXAFS) plots for fresh and 1st cycled p-NVPF and HE-NVPF cathodes. The first peak indicates the V-O/F coordination shells of p-NVPF and HE-NVPF. The radical distance of the V—O/F bond reduces from 1.50 Å for fresh p-NVPF to 1.38 Å the 1st cycled sample, which can be attributed to a slightly higher valence of V after the 1st cycle. The decreased peak intensity for the first V—O/F bond in p-NVPF suggests lattice distortion or phase

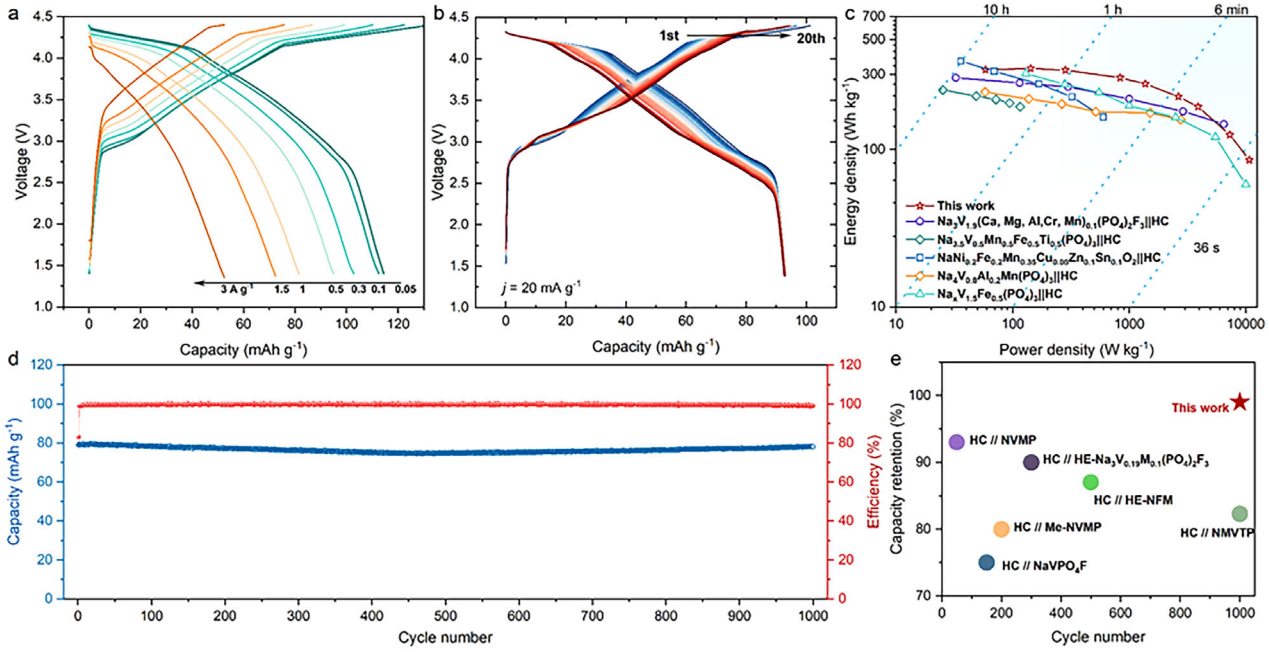

Figure 4. Electrochemical performance of graphite//HE-NVPF full cells. a) Rate capability from 0.05 to 3 A g^{-1}. b) The charge–discharge profiles at 20 mA g^{-1} for 20 cycles. c) Ragone plots of Na-ion full batteries.[10a,f,18] d) Cycling performance at 1 A g^{-1}. e) Summary of full cell electrochemical performance for SIBs.[4b,10a,f,18a,22]

separation after discharging. In contrast, HE-NVPF shows negligible changes in peak position and intensities for the V—O/F coordination shell. Overall, the X-ray characterizations confirm the reversible V redox and stable local structures for HE-NVPF cathodes.

Finally, to demonstrate the practical feasibility of HE-NVPF, a full cell was assembled using the graphite anode, the HE-NVPF cathode, and 1 M $NaPF_6$ diglyme electrolyte. The electrochemical performance is shown in **Figure 4**. It is worth noting that graphite anode undergoing cointercalation reaction in ether-based electrolyte can present excellent cyclability and high-rate capability (Figure S19, Supporting Information),[16] thus it is selected to pair with our fast-charging HE-NVPF cathodes. The 1 M $NaPF_6$ diglyme electrolyte exhibits an electrochemical stability window of 4.6 V (Figure S20, Supporting Information), accommodating the high cutoff voltages (1.4–4.4 V) required for graphite//HE-NVPF full-cells. Prior to assembly, the graphite anodes were pre-activated in Na-metal half cells to form a stable solid-electrolyte interphase. The negative to positive capacity ratio (N/P) was set as 1:4.4, which is significantly lower than these in previous studies, e.g., the N/P ratio = 3/5 for graphite//$Na_{1.5}VPO_{4.8}F_{0.7}$ cells,[16a,17] N/P ratio = 6/5 for hard carbon// $Na_3V_{1.9}$(Ca, Mg, Al, Cr, Mn)$_{0.1}(PO_4)_2F_3$ cells,[10a] and N/P ratio = 8/7 for hard carbon//$Na_{3.5}V_{0.5}Mn_{0.5}Fe_{0.5}Ti_{0.5}(PO_4)_3$ cells.[10f] The low N/P ratio can enhance the practical energy densities for Na-ion full cells without causing Na loss and fast capacity fade. It is worth noting that the ether-based electrolyte enables solvated-Na-ion cointercalation reaction and the formation of sodiophilic ternary graphite intercalation compound (*t*-GIC). The *t*-GIC provides thermodynamically favorable sites for dendrite-free Na metal deposition,[16b] thus enabling the low N/P ratio for graphite//HE-NVPF full cells.

Figure 4a illustrates the rate capability of graphite//HE-NVPF full-cells at increasing current densities from 0.05 A g^{-1} to 3A g^{-1}.They deliver capacities of 114, 112, 103, 95, 82, 72, and 53 mAh g^{-1} at 0.05, 0.1,0.3, 0.5, 1, 1.5, and 3 A g^{-1}, respectively. At a current density of 0.05 A g^{-1}, an average operating voltage of 3.78 V and a competitive energy density of 342 Wh kg^{-1} are achieved based on the total mass of anode and cathode materials. Figure 4b shows the initial 20 cycles' discharging/charging voltage profiles at 20 mA g^{-1}, which maintained the initial capacity by 99.6%. Compared with the state-of-the-art Na-ion full cells, our graphite//HE-NVPF cells show outstanding power densities of 3902, 7296, 10,726 W kg^{-1} at competitive energy densities of 187, 124, and 86 Wh kg^{-1} on base of the total mass of cathode and anode active materials (Figure 4c).[10a,f,18] Notably, the graphite//HE-NVPF cells with power densities of above 10 000 W kg^{-1} under energy density of >100 Wh kg^{-1} surpasses advanced supercapacitors (e.g., 800 W kg^{-1}/88 Wh kg^{-1} for $NiCo(HPO_4)_2 \cdot 3H_2O$//3DPG,[19] 800 W kg^{-1}/51 Wh kg^{-1} for Co_3O_4//RGO,[20] and 997 W kg^{-1}/68 Wh kg^{-1} for SnO_{2-x} NPs@SnO_{2-x}//MnO_2[21]).

Figure 4d shows the long-term cycling performance of graphite//HE-NVPF full cells at 1 A g^{-1} for 1000 cycles. It presents reversible capacities of 78.8 and 78.0 mAh g^{-1} for 1st and 1000th cycles, leading to an extremely high capacity retention of 99%. The cyclic capacities at a moderate current density of 100 mA g^{-1} present negligible capacity fluctuations after 100 cycles (Figure S21, Supporting Information). Figure 4e emphasizes the outstanding electrochemical performance of SIBs with HE-NVPF cathode among its peers.[4b,10a,f,18a,22] Table S3 (Supporting Information) summarizes the battery performance of the representative Na-ion full cells,[10a,f,18] which shows the outstanding energy density and cyclability of our graphite//HE-NVPF cells,

thus demonstrating the practical feasibility of HE-NVPF cathodes in SIBs.

3. Conclusion

In summary, this work introduces a high-entropy doping strategy to develop carbon-free and single-crystal HE-NVPF cathode materials for ultrastable SIBs. By introducing trace amounts of dopants, HE-NVPF achieves high phase purity, no carbon coating, and enhanced ionic/electronic conductivities. Benefiting from the high-entropy effect, HE-NVPF cathodes deliver a high average operation voltage of 4.0 V and an energy density of 532 Wh kg^{-1}. Additionally, it also exhibits excellent crystal stability (75.58% capacity retention at 10 C after 3000 cycles) and remarkable high-rate capability (capacity of 65.55 mAh g^{-1} at 30 C). The superior electrochemical performance of graphite//HE-NVPF full cells demonstrate the practical feasibility of HE-NVPF cathodes in high-power and long-life SIBs. The outstanding electrochemical performance originates from the solid-solution Na storage mechanism and the small volume changes of the HE-NVPF structure. Overall, this work opens a new avenue for building high-entropy doped KTP-typed cathodes in high-performance SIBs.

4. Experimental Section

Synthesis of HE-NVPF: $NaV_{0.95}$(Fe, Mn, Ni, Al, Ca)$_{0.05}PO_4F$ was synthesized by a two-step ion-exchange approach. First, through the hydrothermal method synthesized $NH_4V_{0.95}$(Fe, Mn, Ni, Al, Ca)$_{0.05}PO_4F$ precursor. The $VOSO_4$ (9.5 mmol, Macklin), $FeSO_4{\cdot}7H_2O$ (0.1 mmol, Aladdin), $MnSO_4{\cdot}H_2O$ (0.1 mmol, Aladdin), $NiCl_2{\cdot}6H_2O$ (0.1 mmol, Aladdin), $Al_2(SO_4)_3{\cdot}16H_2O$ (0.05 mmol, Aladdin), $CaCl_2$ (0.1 mmol, Aladdin), $(NH_4)_2HPO_4$ (15 mmol, Aladdin), $NH_4H_2PO_4$ (15 mmol, Aladdin), $N_2H_6SO_4$ (3.75 mmol, Macklin), and NH_4F (20 mmol, Aladdin) were added to the distilled H_2O solution (44 mL) one after another under constant stirring. After the dark-blue suspension formed, transferred it into a 100 mL Teflon-lined stainless-steel autoclave. This autoclave was sealed and heated at 200 °C for 4 h. The result product was collected, then, washed with distilled H_2O and acetone by centrifuge. The precursor was further dried in an 80 °C vacuum oven overnight. The precursor ($NH_4V_{0.95}$(Fe, Mn, Ni, Al, Ca)$_{0.05}PO_4F$) was mixed with sodium glutamate in a molar ratio of 1:5 and annealed at 190 °C under argon for 10 h. Dissolved black gel-like product in distilled H_2O of 80 °C and filtered. Finally, further dried the product and obtain $NaV_{0.95}$(Fe, Mn, Ni, Al, Ca)$_{0.05}PO_4F$ powder. The synthesis process for pristine $NaVPO_4F$ is similar to that of HE-NVPF, except that the first hydrothermal step requires the addition of an extra 0.4 g of CMC-Na to 44 mL of distilled H_2O beforehand.

Material Characterization: The X-ray diffraction patterns were collected on a Rigaku SmartLab 9 kW X-ray diffractometer (Cu Kα radiation, λ = 1.5418 Å, current: 20 mA, voltage: 45 kV) in a scan range (2θ) of 10°–80°. X-ray photoelectron spectroscopy (XPS) was performed on a Thermo Fisher Scientific Nexsa with a monochromatic Al Kα source. The morphology and energy dispersive X-ray spectroscopy (EDS) mapping of the materials were collected on scanning electron microscope (SEM, TESCAN MIRA). A transmission electron microscope (TEM, JEQL 2100F) was used to capture the morphology and EDS mapping of HE-NVPF. Due the electron beam sensitive of the NVPF cathode, the Spectra 300 STEM was used to investigate the atomic-scale arrangement of HE-NVPF. The inductively coupled plasma-optical emission spectroscopy (ICP-OES, Agilent 5110) was carried out to confirm the element compositions of the samples. It is noted that high tolerance of ICP-OES suggests the qualitative nature of the measurement data. In situ XRD patterns were collected on Bruker D8 Advance in a scan range of 13°–45° with 15 min intervals. The cells ran for one charge/discharge cycle at 0.15 C in room temperature. The Rietveld refinement was performed on FullProf.[23] The X-ray absorption spectra (XAS) were collected at the 6D UNIST-PAL beamline in Pohang Light Source (PLS). The data of XAS were performed on Demeter.[24]

Calculation Method: In this work, density functional theory (DFT) calculations of periodic slabs were performed using the Vienna Ab initio Simulation Package.[25] The electron density and system energy were described by the projector augmented-wave (PAW) method combined with the Perdew–Burke–Ernzerhof (PBE) functional.[26] The electronic structure was characterized using the generalized gradient approximation (GGA).[27] A plane-wave cutoff energy of 450 eV was employed with a force convergence criterion of 0.05 eV. All calculations included spin polarization effects. The lattice parameters of $NaVPO_4F$ were fully optimized using a k-point spacing of 0.080 $Å^{-1}$. To investigate high-entropy structures, a fourfold supercell containing 256 atoms were constructed. We generated a dataset of 100 structures with different random doping configurations was generated, performed full geometric optimization on each, and selected the 15 most stable structures to subsequently analyze their electronic structures.

Electrochemical Measurements: The electrochemical measurements were conducted in CR2032 coin-type cells. The active materials, super P, and polyvinylidene fluoride (PVDF) were coated onto Al foil with the mass ratio of 8:1:1 using N-methyl-2-pyrrolidone (NMP) as the solvent and dried under vacuum at 80 °C for 12 h to make a working electrode. The mass loading of active materials is ≈2 mg cm^{-2}. The sodium metal foil was the counter and reference electrode, the glass fiber GF/A is the separator. The electrolyte consisted of 1 M $NaPF_6$ EMC:FEMC: FEC = 2:3:5. The coin-cells were assembled in an argon-filled glovebox with $H_2O$and O_2 lower than 0.1 ppm. The galvanostatic charge–discharge (GCD) measurements were conducted on the battery testing system (Neware) in the voltage range of 2.0–4.5 V versus Na^+/Na. The galvanostatic intermittent titration technique (GITT) were used to investigate the electrode kinetics via calculating Na^+ diffusion coefficients. For full cell fabrication, a graphite slurry, prepared with a mass ratio of graphite to PVDF of 9:1 using NMP as the solvent, was coated onto Cu foil. The coated foil was subsequently dried under vacuum at 80 °C for 12 h. Then the graphite electrode was pre-sodiated to avoid excessive sodium loss of cathode. Using glass fiber GF/A as the separator, the electrolyte is 1 M $NaPF_6$ in diglyme. The voltage window for the full cell test is 1.4–4.4 V.

Supporting Information

Supporting Information is available from the Wiley Online Library or from the author.

Acknowledgements

The work described in this paper was supported by the Innovation and Technology Fund-Innovation and Technology Support Programme (ITF-ITSP) (Project No. ITS/126/21), and Environment and Conservation Fund (Project No. ECF/110/2021) from the Environment and Conversion Fund Committee of Hong Kong, SAR, Research Institute for Advanced Manufacturing (Project No. 1-CD9C) and Research Institute for Smart Energy (Project No. U-CDCK) at the Hong Kong Polytechnic University, and the National R&D Program through the National Research Foundation of Korea (NRF) funded by Ministry of Science and ICT (No. RS-2024-00408156).

Conflict of Interest

The authors declare no conflict of interest.

Author Contributions

Z.L.X. conceived the concept. K.Y. carried out the DFT calculations. Z.S. and Z.C. performed the TEM experiments and analyses. S.S. and K.Y.P.

conducted the ex situ X-ray absorption experiments. Y.H. and L.L. tested electrochemical performances and prepared the ex situ samples. X.P., R.L., and Y.H. carried out the in situ XRD test and XRD Rietveld refinements. Z.L.X. and H.H. supervised the research. Z.L.X. revised the manuscript prepared by Y.H.

Data Availability Statement

The data that support the findings of this study are available from the corresponding author upon reasonable request.

Keywords

high-entropy effect, long-life cycling stability, NASICON cathodes, sodium-ion batteries

Received: May 16, 2025
Revised: June 9, 2025
Published online: July 9, 2025

[1] a) A. Rudola, R. Sayers, C. J. Wright, J. Barker, *Nat. Energy* **2023**, *8*, 215; b) K. Kubota, M. Dahbi, T. Hosaka, S. Kumakura, S. Komaba, *Chem. Rec.* **2018**, *18*, 459; c) H. Wang, E. Matios, J. Luo, W. Li, *Chem. Soc. Rev.* **2020**, *49*, 3783.

[2] a) J.-Y. Hwang, J. Kim, T.-Y. Yu, Y.-K. Sun, *Adv. Energy Mater.* **2019**, *9*, 1803346; b) M. Ren, S. Zhao, S. Gao, T. Zhang, M. Hou, W. Zhang, K. Feng, J. Zhong, W. Hua, S. Indris, K. Zhang, J. Chen, F. Li, *J. Am. Chem. Soc.* **2023**, *145*, 224; c) T.-Y. Yu, H.-H. Ryu, G. Han, Y.-K. Sun, *Adv. Energy Mater.* **2020**, *10*, 2001609.

[3] a) Y. Ma, Y. Hu, Y. Pramudya, T. Diemant, Q. Wang, D. Goonetilleke, Y. Tang, B. Zhou, H. Hahn, W. Wenzel, M. Fichtner, Y. Ma, B. Breitung, T. Brezesinski, *Adv. Funct. Mater.* **2022**, *32*, 2202372; b) J. Qian, C. Wu, Y. Cao, Z. Ma, Y. Huang, X. Ai, H. Yang, *Adv. Energy Mater.* **2018**, *8*, 1702619.

[4] a) Y.-U. Park, D.-H. Seo, H. Kim, J. Kim, S. Lee, B. Kim, K. Kang, *Adv. Funct. Mater.* **2014**, *24*, 4603; b) S. D. Shraer, N. D. Luchinin, I. A. Trussov, D. A. Aksyonov, A. V. Morozov, S. V. Ryazantsev, A. R. Iarchuk, P. A. Morozova, V. A. Nikitina, K. J. Stevenson, E. V. Antipov, A. M. Abakumov, S. S. Fedotov, *Nat. Commun.* **2022**, *13*, 4097; c) L. Liang, X. Li, F. Zhao, J. Zhang, Y. Liu, L. Hou, C. Yuan, *Adv. Energy Mater.* **2021**, *11*, 2100287; d) T. Jin, H. Li, K. Zhu, P.-F. Wang, P. Liu, L. Jiao, *Chem. Soc. Rev.* **2020**, *49*, 2342.

[5] Y. Fang, L. Xiao, X. Ai, Y. Cao, H. Yang, *Adv. Mater.* **2015**, *27*, 5895.

[6] G. Yan, S. Mariyappan, G. Rousse, Q. Jacquet, M. Deschamps, R. David, B. Mirvaux, J. W. Freeland, J.-M. Tarascon, *Nat. Commun.* **2019**, *10*, 585.

[7] N. Recham, G. Rousse, M. T. Sougrati, J.-N. Chotard, C. Frayret, S. Mariyappan, B. C. Melot, J.-C. Jumas, J.-M. Tarascon, *Chem. Mater.* **2012**, *24*, 4363.

[8] X. Liang, J.-Y. Hwang, Y.-K. Sun, *Adv. Energy Mater.* **2023**, *13*, 2301975.

[9] a) Q. Wei, X. Chang, J. Wang, T. Huang, X. Huang, J. Yu, H. Zheng, J.-h. Chen, D.-L. Peng, *Adv. Mater.* **2022**, *34*, 2108304; b) Y. Subramanian, W. Oh, W. Choi, H. Lee, M. Jeong, R. Thangavel, W.-S. Yoon, *Chem. Eng. J.* **2021**, *403*, 126291; c) L. Shen, Y. Li, S. Roy, X. Yin, W. Liu, S. Shi, X. Wang, X. Yin, J. Zhang, Y. Zhao, *Chin. Chem. Lett.* **2021**, *32*, 3570.

[10] a) Z. Y. Gu, J. Z. Guo, J. M. Cao, X. T. Wang, X. X. Zhao, X. Y. Zheng, W. H. Li, Z. H. Sun, H. J. Liang, X. L. Wu, *Adv. Mater.* **2022**, *34*, 2110108; b) L. Yao, P. Zou, C. Wang, J. Jiang, L. Ma, S. Tan, K. A. Beyer, F. Xu, E. Hu, H. L. Xin, *Adv. Energy Mater.* **2022**, *12*, 2201989; c) S. Ma, P. Zou, H. L. Xin, *Mater. Today Energy* **2023**, *38*, 101446; d) F. Ding, P. Ji, Z. Han, X. Hou, Y. Yang, Z. Hu, Y. Niu, Y. Liu, J. Zhang, X. Rong, Y. Lu, H. Mao, D. Su, L. Chen, Y.-S. Hu, *Nat. Energy* **2024**, *9*, 1529; e) C. Zhao, C. Wang, X. Liu, I. Hwang, T. Li, X. Zhou, J. Diao, J. Deng, Y. Qin, Z. Yang, G. Wang, W. Xu, C. Sun, L. Wu, W. Cha, I. Robinson, R. Harder, Y. Jiang, T. Bicer, J.-T. Li, W. Lu, L. Li, Y. Liu, S.-G. Sun, G.-L. Xu, K. Amine, *Nat. Energy* **2024**, *9*, 345; f) M. Li, C. Sun, X. Yuan, Y. Li, Y. Yuan, H. Jin, J. Lu, Y. Zhao, *Adv. Funct. Mater.* **2024**, *34*, 2314019; g) H. Gao, J. Li, F. Zhang, C. Li, J. Xiao, X. Nie, G. Zhang, Y. Xiao, D. Zhang, X. Guo, Y. Wang, Y. M. Kang, G. Wang, H. Liu, *Adv. Energy Mater.* **2024**, *14*, 2304529; h) W. Zheng, G. Liang, Q. Liu, J. Li, J. A. Yuwono, S. Zhang, V. K. Peterson, Z. Guo, *Joule* **2023**, *7*, 2732; i) R. Zhang, C. Wang, P. Zou, R. Lin, L. Ma, L. Yin, T. Li, W. Xu, H. Jia, Q. Li, S. Sainio, K. Kisslinger, S. E. Trask, S. N. Ehrlich, Y. Yang, A. M. Kiss, M. Ge, B. J. Polzin, S. J. Lee, W. Xu, Y. Ren, H. L. Xin, *Nature* **2022**, *610*, 67; j) H. Li, X. Sun, H. Huang, *Prog. Mater. Sci.* **2025**, *148*, 101382; k) G. Su, Y. Wang, J. Mu, Y. Ren, P. Yue, W. Ji, L. Liang, L. Hou, M. Chen, C. Yuan, *Adv. Energy Mater.* **2025**, *15*, 2403282; l) Z. Chen, Y. Wu, Q. Yang, T. Huang, S. Li, S. Shi, Y. Zhang, M. Fan, T. Huo, X. Bai, G. Yu, M. Li, W. Zhang, X. Zhou, L. Li, K. Lei, S. Dou, S. Zheng, *Nano Res.* **2025**, *18*, 94907607; m) Z. Hao, X. Shi, W. Zhu, Z. Yang, X. Zhou, C. Wang, L. Li, W. Hua, C.-Q. Ma, S. Chou, *ACS Nano* **2024**, *18*, 9354.

[11] R. Shannon, *Acta Cryst.* **1976**, *A32*, 751.

[12] J. Wang, X. Lin, X. Luo, Y. Long, *Chem. Eng. J.* **2014**, *252*, 415.

[13] A. Manthiram, *Nat. Commun.* **2020**, *11*, 1550.

[14] M. Li, H. Zhuo, J. Lei, Y. Guo, Y. Yuan, K. Wang, Z. Liao, W. Xia, D. Geng, X. Sun, J. Hu, B. Xiao, *Nat. Commun.* **2025**, *16*, 2010.

[15] a) P. Chaurand, J. Rose, V. Briois, M. Salome, O. Proux, V. Nassif, L. Olivi, J. Susini, J.-L. Hazemann, J.-Y. Bottero, *J. Phys. Chem. B* **2007**, *111*, 5101; b) J. Wong, F. W. Lytle, R. P. Messmer, D. H. Maylotte, *Phys. Rev. B* **1984**, *30*, 5596; c) R. Wernert, L. H. B. Nguyen, E. Petit, P. S. Camacho, A. Iadecola, A. Longo, F. Fauth, L. Stievano, L. Monconduit, D. Carlier, L. Croguennec, *Chem. Mater.* **2022**, *34*, 4523.

[16] a) Z.-L. Xu, G. Yoon, K.-Y. Park, H. Park, O. Tamwattana, S. Joo Kim, W. M. Seong, K. Kang, *Nat. Commun.* **2019**, *10*, 2598; b) L. Lyu, Y. Zheng, Y. Hua, J. Li, Y. Yi, Y. Sun, Z. L. Xu, *Angew. Chem., Int. Ed.* **2024**, *63*, 202410253.

[17] a) H. Kim, J. Hong, Y.-U. Park, J. Kim, I. Hwang, K. Kang, *Adv. Funct. Mater.* **2015**, *25*, 534; b) Z. Zhu, F. Cheng, Z. Hu, Z. Niu, J. Chen, *J. Power Sources* **2015**, *293*, 626; c) I. Hasa, X. Dou, D. Buchholz, Y. Shao-Horn, J. Hassoun, S. Passerini, B. Scrosati, *J. Power Sources* **2016**, *310*, 26.

[18] a) B. Wang, J. Ma, K. Wang, D. Wang, G. Xu, X. Wang, Z. Hu, C.-W. Pao, J.-L. Chen, L. Du, X. Du, G. Cui, *Adv. Energy Mater.* **2024**, *14*, 2401090; b) C. Xu, R. Xiao, J. Zhao, F. Ding, Y. Yang, X. Rong, X. Guo, C. Yang, H. Liu, B. Zhong, Y.-S. Hu, *ACS Energy Lett.* **2022**, *7*, 97; c) Y. Zhou, G. Xu, J. Lin, Y. Zhang, G. Fang, J. Zhou, X. Cao, S. Liang, *Adv. Mater.* **2023**, *35*, 2304428.

[19] J. Huang, Y. Xiong, Z. Peng, L. Chen, L. Wang, Y. Xu, L. Tan, K. Yuan, Y. Chen, *ACS Nano* **2020**, *14*, 14201.

[20] J. Huang, Y. Xiao, Z. Peng, Y. Xu, L. Li, L. Tan, K. Yuan, Y. Chen, *Adv. Sci.* **2019**, *6*, 1900107.

[21] B. Liu, S. Sun, R. Jia, H. Zhang, X. Zhu, C. Zhang, J. Xu, T. Zhai, H. Xia, *Adv. Funct. Mater.* **2020**, *30*, 1909546.

[22] a) M. Li, C. Sun, Q. Ni, Z. Sun, Y. Liu, Y. Li, L. Li, H. Jin, Y. Zhao, *Adv. Energy Mater.* **2023**, *13*, 2203971; b) L. Zhu, M. Wang, S. Xiang, D. Sun, Y. Tang, H. Wang, *Adv. Energy Mater.* **2023**, *13*, 2302046.

[23] J. Rodríguez-Carvajal, *Physica. B Condens. Matter.* **1993**, *192*, 55.

[24] B. Ravel, M. Newville, *J. Synchrotron Radiat.* **2005**, *12*, 537.

[25] a) G. Kresse, J. Furthmüller, *Comp. Mater. Sci.* **1996**, *6*, 15; b) G. Kresse, J. Furthmüller, *Phys. Rev. B* **1996**, *54*, 11169; c) G. Kresse, J. Hafner, *Phys. Rev. B* **1993**, *47*, 558; d) G. Kresse, J. Hafner, *Phys. Rev. B* **1994**, *49*, 14251.

[26] a) P. E. Blöchl, *Phys. Rev. B* **1994**, *50*, 17953; b) G. Kresse, D. Joubert, *Phys. Rev. B* **1999**, *59*, 1758.

[27] J. P. Perdew, K. Burke, M. Ernzerhof, *Phys. Rev. Lett.* **1996**, *77*, 3865.